

THERMAL EVAPORATED WO₃ NANOPARTICLES FILM UNDER DIFFERENT EVAPORATION PRESSURES FOR NO₂ SENSING

M. BEKRI^{a*}, N. M. SHAALAN^{b*}, A. S. AHMED^a

^aPhysics Department, College of Science and Arts, King Abdulaziz University, Rabigh 21911, KSA;

^bPhysics Department, Faculty of Science, Assiut University, 71516 Assiut, Egypt.

In this study, the fabrication of tungsten oxide (WO₃) nanoparticles in effective size using thermal evaporation method under different conditions was reported. The fabricated WO₃ were examined and characterized by X-ray diffraction, and field-emission scanning electron microscope. Our examination showed that WO₃ nanoparticles with a monoclinic structure were assembled with large quantity. Both of the crystallite and particle size are increase with increasing the evaporation pressure and substrate temperature. In addition, we check the ability of the fabricated WO₃ for nitrogen dioxide (NO₂) sensing at different operating temperatures. The gas sensing properties showed highest sensitivity of 204 to 1 ppm NO₂ at an operating temperature of 140°C, which was observed for a sensor made of particles as small as 12±3 nm. The electrical resistance of WO₃ showed a unique thermal behavior of the fabricated sensor.

(Received April 5, 2015; Accepted June 5, 2015)

Keywords: Thermal evaporation, nanostructure, tungsten oxide, gas sensing

1. Introduction

Fabrication and controlling the growth of semiconducting oxides nanostructures have much attention in the field of materials science due to their applications in microelectronics, energy, optoelectronic, electrochromic devices etc. Among these semiconducting oxides, tungsten trioxide (WO₃) is an n-type semiconductor and it exhibits a wide variety of novel properties particularly in thin film form which useful for advanced technological applications.

Different physical and chemical methods can be used for WO₃ thin films preparation such as thermal evaporation^[1], sol-gel method^[2], electron beam evaporation^[3], chemical vapour deposition^[4], electrochemical deposition^[5], electrochemical anodization^[6] and laser deposition^[7]. Each method leads to different composition, structure and morphology, and shape which reflect the performance of the product. In this work, we used the simplified thermal evaporation method due its simplicity, an effective cost and easy controlled.

Among its applications, WO₃ have been used for detecting a variety of gases, such as nitrogen dioxide (NO₂), carbon monoxide (CO), hydrogen (H₂), sulfur dioxide (SO₂), and ammonia (NH₃). In particular, nanostructured WO₃ like nanospheres and nanowires as it provide a high surface area on a foot print resulting on a high sensitive gas sensor, which are unattainable by other conventional materials. Various shapes and morphology of WO₃ nanostructured such as nanorods, nanowires, nanotubes, nanoflakes and nanodisks have been synthesized by mentioned methods.

NO₂ which is an indicator of various kinds of vehicle emission, internal combustion engines, thermal power stations, etc. ^[8]. NO₂ is also a precursor for a number of harmful secondary air pollutants. Health risks result due to NO₂ itself and its reaction products, such as O₃. It causes an impairing in the lung function and respiratory system with long-term exposure ^[9].

*Corresponding author: nshaalan@aun.edu.eg

It also irritates the nose, eye, and throat, creating a potential risk for overexposure. NO₂ gas should be easily detected and controlled at harmless levels.

Many works done in this area has proven that the gas sensing properties and performance of WO₃ are dramatically affected by the morphology of nanomaterial and reducing the grain size^[10-15]. The grain size relative to the depth of depletion layer is the important parameter influencing the sensing property of the semiconductor^[14,16-20]. It is assured that a high response can be obtained if the crystallite size is prepared less than Debye length of the nanomaterials^[20], which is the main aim of the present research work to reach it. Yamazoe and Shimano have theoretically reported two types of depletion for the nanomaterials; regional and volume depletion^[21]. The particles have volume depletion in air or in the presence of gas showed the highest response to the oxidizing gas. Thus, its needed to prepare WO₃ nanoparticles with size less or equal to the Debye length, obtaining a region of volume depletion when the gas is adsorbed on the surface^[18,19]. The structural parameters such as dislocation density, microstrain, and crystallite size in the materials can be quantified by X-ray diffraction (XRD) technique^[22-24]. To obtain an accurate value of the grain size a correction for the broadening is considered in the present work. The investigation of such parameters is important for correlating between the materials structures and to their technological applications.

Herein, we report on a highly sensitive NO₂ sensor using WO₃ nanoparticles and their response improvement by reducing their size. For this purpose, WO₃ nanoparticles were prepared via a thermal evaporation method at different evaporation pressures and temperatures. The prepared materials are characterized by X-ray diffractometer, Scanning electron microscope (SEM), and gas sensing system. Furthermore, the XRD broadening that resultant from crystallite size and that resultant from the microstrain was discussed. In addition, the influence of the quantum size effect of these nanoparticles on the resistance of device and sensing properties to NO₂ gas was presented.

2. Experimental procedures

2.1 WO₃ fabrication

Five different samples were prepared by thermal evaporation method under different conditions as shown in Table 1. The main source of WO₃ was a tungsten filament of 5mm diameter, 150-mm length, and purity of 99.95%. The filament was fixed on two electrodes of AC-electric source. An electric heater was directly fixed upon a silicon substrate which was fixed on the tungsten filament, as outlined schematically in Fig. 1. To carry out the experiment the chamber was first evacuated and kept at the prescribed pressure of ambient air by using a rotary vacuum pump, and the substrate was heated from room temperature (RT) to the desirable temperature and maintained at this temperature during the evaporation of the filament. After the deposition completed the substrate was then cooled to RT, leading to a substrate surface coated with a thick film of WO₃ products. WO₃ products were obtained with a substrate temperature of 500 and 700°C, while the ambient pressures changed from about 4 to 1 Torr.

Table 1: Shows the preparation conditions of temperature and pressure.

Sample	Preparation conditions	
	Evaporation pressure (Torr)	Substrate temperature (°C)
S ₁	4	500
S ₂	3	
S ₃	2	
S ₄	1	
S ₅	2	700

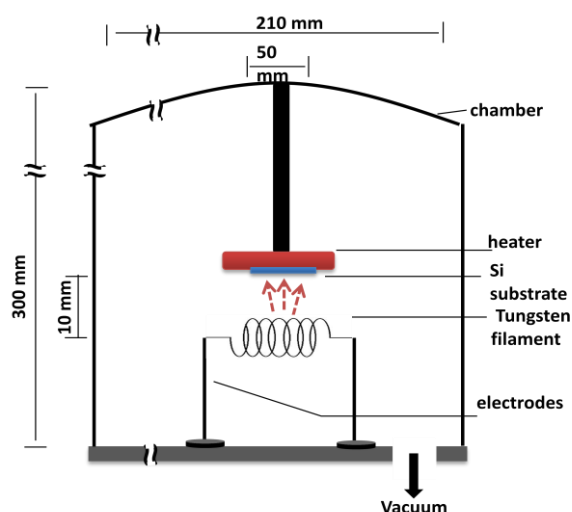


Fig. 1: Schematic diagram of the apparatus used for the formation of WO_3 nanoparticles by thermal evaporation method.

2.2 Characterization of WO_3 nanoparticles

The structural parameters of the obtained products were investigated by X-ray diffraction (XRD). The crystallite size was estimated from XRD pattern employing equations reported in Ref. [22] and Scherrer formula [25]. The morphology of WO_3 products was examined by field-emission scanning electron microscope (FE-SEM). FE-SEM observation was carried out for the film grown on the initial silicon substrate. A JEOL-6700F instrument operated at 10 kV was used for SEM observation. ImageJ Java image-processing software (Version 1.37 for Windows) was used for quantitative analysis of WO_3 structures.

2.3 Gas sensing measurements

For gas sensor fabrication, few drops of ethanol suspended with WO_3 nanoparticles (540 μg) were deposited on a pair of Au electrodes with a thickness of 100 nm and a gap length of 300 μm . In order to investigate NO_2 gas sensing properties, the sensors were placed in a silica tube which containing a small heater fixed beneath the sensor, see Fig. 2. The sensor was heated locally at operating temperatures varied from 70 up to 300°C. Dry synthetic air, mixed with a concentration of NO_2 gas, was passed at a rate of 200 ml/min through a mass flow controller (Horiba-N100-series-MGR). The sensor response (S) is estimated as the ratio of electrical resistance, R_g/R_a , while the sensitivity, $\frac{R_g - R_a}{R_a}$, where R_a is the electrical resistance before introducing gas, and R_g the maximum electrical resistance after introducing gas.

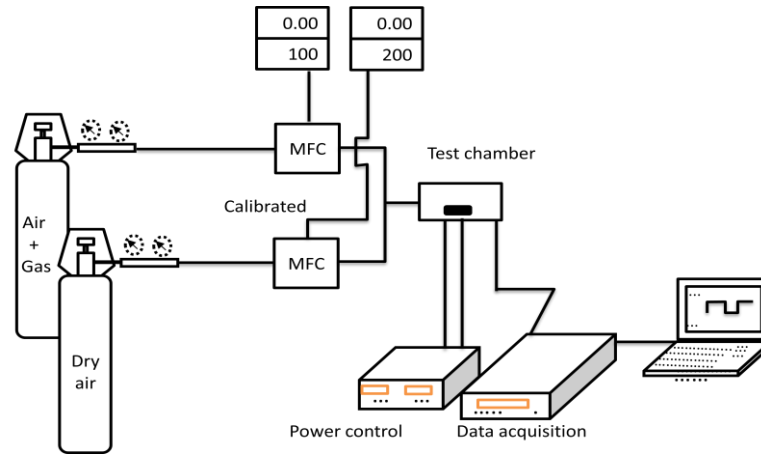


Fig. 2: Schematic shows apparatus that used for the measurement of gas sensing properties; consists of gas cylinders, Horiba mass flow controller, computerized Aligent data acquisition, and power control.

3. Result and discussions

3.1 Crystal structure and morphology

Fig. 3 show XRD patterns which reveals that the products consisted of the polycrystalline monoclinic phase of WO_3 (JCPDS card no. 43-1035), and the preferred crystal orientations are (002), (020), and (200) planes. As observed from this figure, most of the lines indicated in the standard card were observed in the experimental charts. As well, the broadening curve extended by increasing the evaporation pressure from 1 to 4 Torr for samples prepared at 500°C -substrate temperature. This behavior can be ascribed to changes in the crystallite size of WO_3 , resulting on a small crystallite size, or microstrain. The calculation of the average crystallite size and microstrains for the fabricated WO_3 products is not highly expectable due to the overlapping of peaks. Therefore, the calculation of crystallite size and microstrain were performed, to get the best results based on the approximation presented in Ref^[22] for the selected reflections, $\theta_1 = 11.7^\circ$ and $\theta_2 = 16.9^\circ$, as follows:

$$\frac{\beta_2}{\beta_1} = \frac{\{[V(m_1/\beta_1)]+[2(n_1/\beta_1)W]\}^2}{[V(m_1/\beta_1)]+[4(n_1/\beta_1)W]} \quad (1)$$

$$V = \frac{m_2}{m_1} = \frac{\cos \theta_2}{\cos \theta_1}, \text{ and } W = \frac{n_2}{n_1} = \frac{\tan \theta_1}{\tan \theta_2} \quad (2)$$

where m_1 and m_2 are the broadening due to the crystallite size, n_1 and n_2 the broadening due to the strain, β_1 and β_2 the total broadening for the peaks at $\theta_1=11.7^\circ$ and $\theta_2=16.9^\circ$, respectively. To determine the values of m and n graphically, it is logically that (n_1/β_1) takes the values from 0 to 1, and then (m_1/β_1) can be calculated from Eq. (3):

$$\frac{m_1}{\beta_1} = \frac{1}{2} \left[1 - 4 \frac{n_1}{\beta_1} + \sqrt{1 + 8 \left(\frac{n_1}{\beta_1} \right)} \right] \quad (3)$$

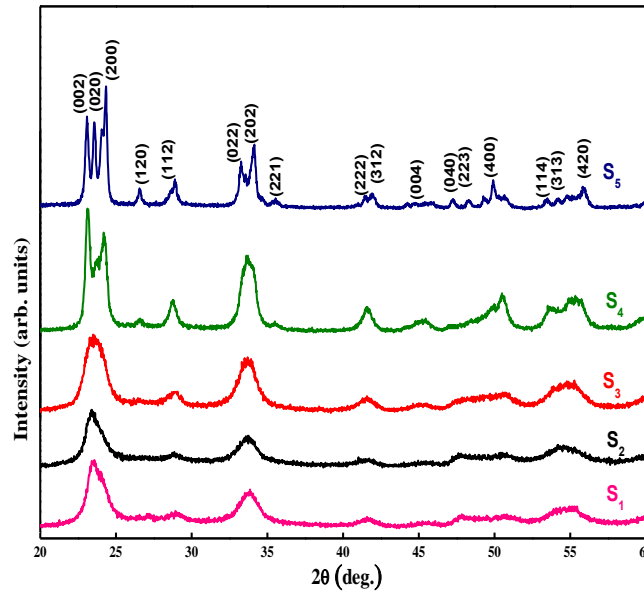


Fig. 3: XRD patterns of WO_3 nanoparticles prepared at different evaporation pressure and substrate temperature, respectively, as S_1 : 4 Torr/500 C, S_2 : 3 Torr/500 C, S_3 : 2 Torr/500 C, S_4 : 1 Torr /500 C, and S_5 : 2 Torr /700 C.

The ratio between the total broadening (β_2/β_1) can be calculated by using Eq. (1). The calculated (m_1/β_1) and (n_1/β_1) are plotted against (β_2/β_1) as shown in Fig. 4. Referring to $(\beta_2/\beta_1)_{\text{exp}}$ reported in Table 2 for XRD charts, the corresponding experimental values of $(m_1)_{\text{exp}}$ and $(n_1)_{\text{exp}}$ are estimated from the plotted graph. Therefore, the crystallite size can be calculated by using Scherrer formula [25]:

$$D = \frac{K\lambda}{\beta \cos \theta} \quad (4)$$

Where β is the full width at half maximum (in radian). K is a constant close to unity, λ is the wavelength of the X-radiation (Cu-K α 0.154 nm), and θ is the Bragg angle of the reflection. The average crystallite size, D , was calculated using Eq. (4) after replacing the total broadening, β , by the broadening due to the crystallite size, m . As well as, the relationship between microstrain, ϵ , and the broadening due to microdeformation, n_1 , is given in the following equation [26]:

$$\epsilon_r = \frac{n}{4 \tan \theta} \quad (5)$$

Table 2 shows the values of $(m_1/\beta_1)_{\text{exp}}$ which obtained from Fig. 4. These values are 0.97, 0.82, 0.86, and 0.36 for samples S_1 , S_2 , S_3 , and S_4 , respectively. The corresponding crystallite sizes are 6.40, 8.19, 8.32, and 27.50 nm, respectively. It can be depicted that the crystallite size increases with decreasing the evaporation pressure, and the crystallite size is significantly larger for S_4 , exceptionally S_5 which has the largest particle observed from SEM. The average crystallite size for sample S_5 is difficult to determine due to the overlapping of peaks as observed in XRD chart.

Table 2: Shows the crystallite size and microstrain calculated using a graph of the approximation method.

Samples	$\beta_1 \times 10^{-2}$ $2\theta = 23.6^\circ$	$\beta_2 \times 10^{-2}$ $2\theta = 33.7^\circ$	β_2/β_1	m_1/β_1	n_1/β_1	m_1 $\times 10^{-2}$	n_1 $\times 10^{-2}$	Crystallite size (nm)	Strain $\times 10^{-3}$
S ₁	2.51	2.61	1.04	0.97	0.10	2.43	0.25	6.40	3.02
S ₂	2.35	2.65	1.12	0.82	0.30	1.92	0.70	8.19	8.52
S ₃	2.20	2.49	1.11	0.86	0.25	1.89	0.55	8.32	6.64
S ₄	1.50	1.86	1.33	0.38	0.7	0.57	1.05	27.5	12.68

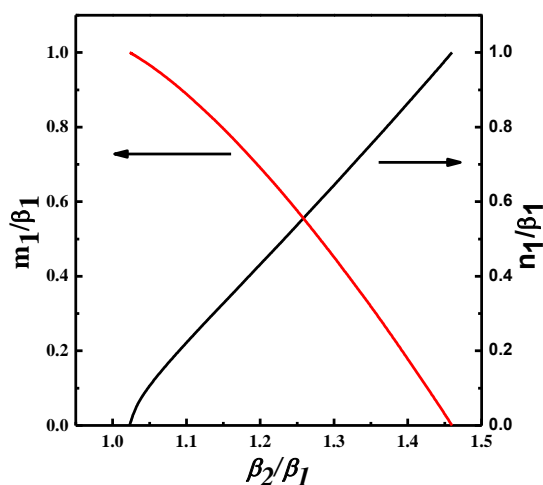


Fig. 4: The calculated (m_1/β_1) and (n_1/β_1) versus (β_2/β_1) based on the theoretical calculations.

The particle size has been investigated using SEM, as shown in Fig. 5. The particles shape are almost spherical-like and in the size of nanoparticles. The estimated particle size rang are 12 ± 3 , 13 ± 4 , 16 ± 6 , 21 ± 3 , and 47 ± 10 nm for samples S₁, S₂, S₃, S₄ and S₅, respectively. The average particle size is decreases as the evaporation pressure increases from 1 to 4 Torr. Similar behavior was reported for thermally evaporated WO₃ nanoparticles at evaporation pressure from 7.5 to 75 Torr at Ref. [14]. These observed values are close to those calculated values of the crystallite size from XRD by using the approximation, indicating that the observed particle is roughly composite of one crystallite. The sample S₅ has the larger value of particle size (≈ 50 nm) because it has higher substrate temperature, which causes the aggregation of the nuclei to be rapid and increases the growth and crystallinity of product as indicated from the XRD charts.

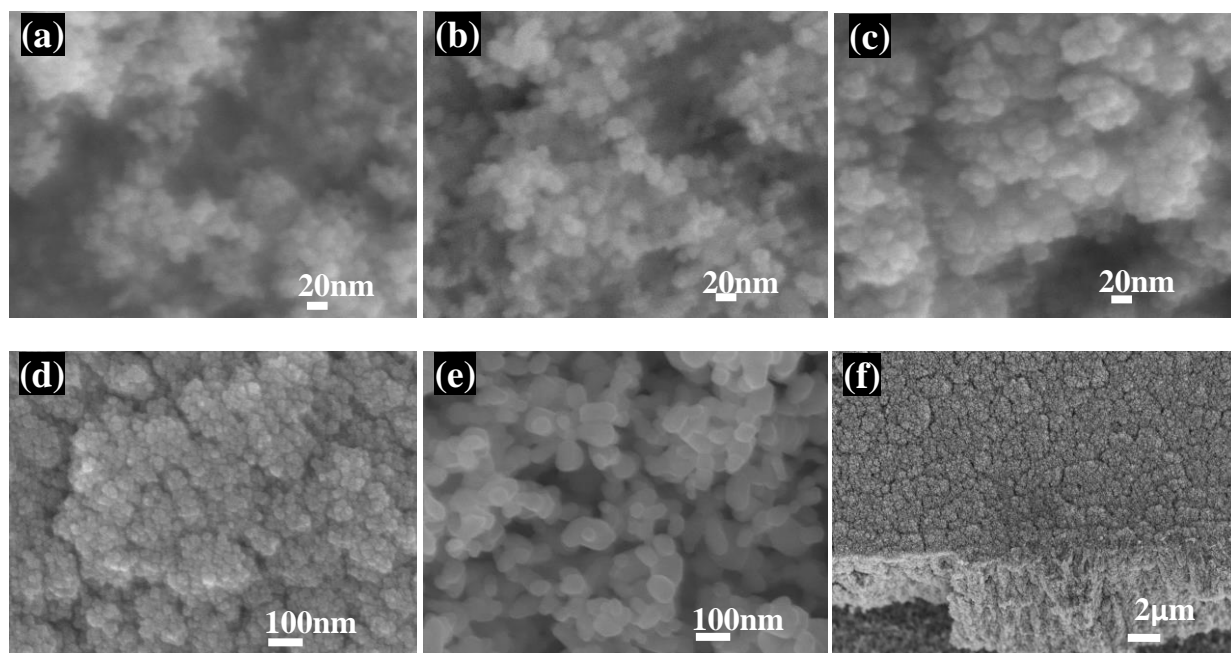


Fig. 5: SEM images show top view of WO_3 nanoparticles for sample (a) S_1 , (b) S_2 , (c) S_3 , (d) S_4 , (e) S_5 , and (f) tilted view of sample S_4 .

Table 2 summarizes the values of $(n_1/\beta_1)_{exp}$ which obtained from Fig. 4. The values are 0.10, 0.30, 0.25, and 0.7 for S_1 , S_2 , S_3 , and S_4 , respectively. The corresponding calculated microstrains are 3.02×10^{-3} , 8.52×10^{-3} , 6.64×10^{-3} , and 12.68×10^{-3} ; see Table 2, indicating that the microstrain was greatly increased with decreasing the evaporation pressure. It is known that film grown by physical vapor deposition techniques is rather stressed. The stress might be compressive or tensile, which is caused by the non-equilibrium microstructure formations. Since the microstrain increases with evaporation pressure decrease, thus the tensile stress is expected.

3.2 NO_2 sensing properties

The electrical resistance and sensor response of WO_3 nanoparticles to NO_2 gas were presented in Fig. 6(a-c). The gas response was defined as the ratio between R_g and R_a . Therefore, the investigation of NO_2 sensing composed of two parts: studying the resistance of the WO_3 exposed to a flow of synthetic air, and then an examination of the sensing ability toward NO_2 , which is an important for the monitoring of air quality in urban locations. It is well known that the resistance of the oxide is affected by the adsorption of reducing or oxidizing gases near its surface. Two types of gas adsorption occurred onto the surface; namely physical and chemical adsorptions. In the physisorption the bonding is weak and the Vander Waals interactions are responsible for this bonding, while in the chemisorption the bonding is strong and involving orbital overlap and charge transfer [27]. In Fig. 6, the shown thermal behavior of sensor resistance accompanied with the sensor response is consisting of the two or three regions; and it seems that the behavior remains constant even after the exposure to the gas.

As well known that WO_3 is n-type semiconductor, and its gas-sensing property belongs to the surface-controlled type, and the change of resistance depends on temperature, species and amount of chemisorbed oxygen onto the surface. The intrinsic resistance of semiconductor has a thermal behavior according to Eq. (6):

$$R = R_o \exp\left(\frac{eV_s}{RT}\right) \quad (6)$$

where V_s is double Schottky barrier height, RT is thermal energy and R_0 is resistance at $V_s=0$. From another side, the oxygen is adsorbed on the surface of the semiconductor as different species with increasing surface temperature. The adsorbates act as surface states by capturing electrons, which are held to the surface by electrostatic attraction; this mechanism causes the resistance of the semiconductor to increase despite a temperature increase^[28]. Hence, every grain has a depletion layer near the surface, and the depth of this layer depends on the surface coverage of states and intrinsic electron concentration in the bulk^[29]. The curves, Figs. 6, presented in this study show a unique behavior due to the competition between adsorbed species and capture of electrons.

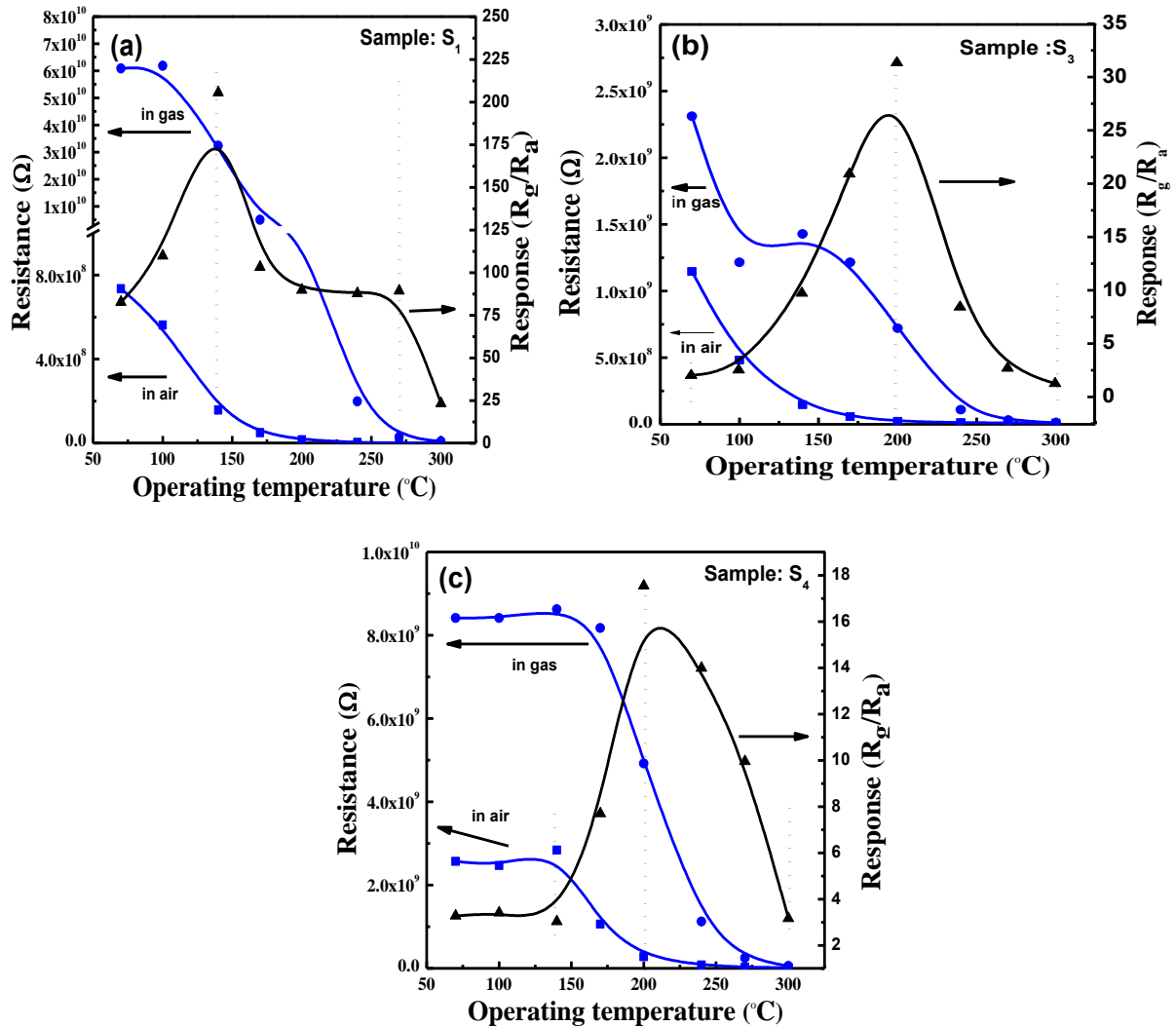


Fig. 6: Thermal behavior of the electric resistance and response of WO_3 device before and after exposure to gas. Response is estimated to ward 1 ppm NO_2 as a function of operating temperature.

The thermal behavior of the resistance was observed in air atmosphere as well as in gas presence. In the case of sample S_1 which has the smallest particle, the resistance is significantly controlled by changing temperature at lower temperatures, while it is temperature-independent at higher ones. Similar behavior is observed for sample S_3 , but the temperature-independent of resistance began early as 150°C . This behavior is common for S_4 , S_3 and S_1 , but the resistance of S_4 is temperature-independent at lower temperatures, while it is temperature-dependent into a median range of temperature. Yamazoe et al.^[30] observed to some extent a similar behavior of resistance for tin oxide thick film, and for deep understanding of this behavior they changed the

atmosphere from air to nitrogen. They stated that with decreasing oxygen partial pressure, the whole resistance went down remarkably, keeping the borders among three regions almost unchanged, until it reached an almost flat one in nitrogen atmosphere. Thus, they have ascribed this unique thermal behavior of sensor resistance to the presence of oxygen in the atmosphere, confirming that the competition between oxygen species and capture electrons decided the thermal behavior of resistance.

The calculated sensor response to 1 ppm NO_2 is also shown in Fig.6. The temperature-dependence of response goes through a rather broadening peak on raising the particle size. The response peak slightly shifted toward a lower operating temperature for the smallest particles e.g. S_1 . Such response behavior has been ascribed to the change of nanostructure size, which can lead to a change in the intensity and the peak position of the sensor response. The change of sensor response in correlation with the thermal behavior or resistance is interesting. The sensor response first increases toward high values in the temperature-dependent region of resistance. In contrary, the response gradually decreases to low values in the temperature-independent region of resistance. This behavior can be ascribed to the transformation of adsorbed oxygen and nitrogen dioxide molecules to their species ions. As stated above the oxygen adsorb onto the surface in various forms of O_2 , O_2^- and O^- depending on the surface temperature. In the range of RT to 200°C , O_2 molecules and O_2^- ions dominate, therefore NO_2 directly react with the surface of semiconductor^[31]. So that the following reaction takes place on the surface of the WO_3 semiconductor:



Due to the oxidation performance of NO_2 , which forms a deeper acceptor level (NO_2^-), NO_2^- ions gradually dominate and control the gas sensing properties of WO_3 , resulting in a gradual increase in the sensor response. With temperature above 200°C , another transformation of oxygen ($O_2^- + e^- \rightarrow O^-$) ions progressively dominate, and the consequent reaction:



takes place and dominates even if NO_2^- is still slightly formed, resulting in a critical transition and gradual reduction in the sensor response. Due to the reaction (7) mechanism of NO_2 with WO_3 , the maximum response was obtained for relative low temperatures.

Table 3: Shows a statistically measured particle size of samples using the SEM micrographs.

sample	Crystallite size (nm)	Average particle size (nm)
S_1	6.40	13.5
S_2	8.19	15
S_3	8.32	19
S_4	27.5	22
S_5	---	52

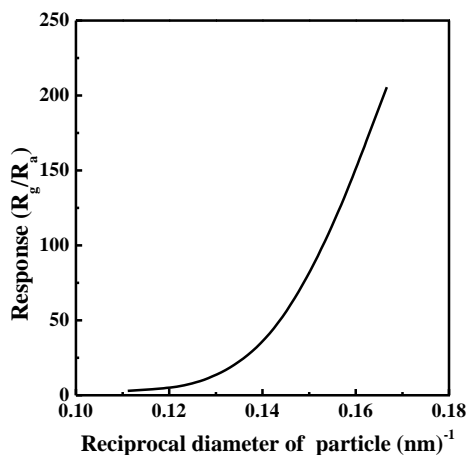


Fig. 7: Shows the height response of WO_3 nanoparticles versus their reciprocal diameter.

Fig.7 shows the response toward 1 ppm nitrogen dioxide as a function of the reciprocal diameter at 140°C-operating temperature. The highest value of the response is observed for the smallest particle. This behavior can be explained by the extremely high surface-to-volume ratio of the nanoparticles with respect to the polycrystalline structure, which causes an increase in the number of active sites.

4. Conclusion

In summary, a developed method of thermal evaporation under low pressure was presented for fabrication of high quality WO_3 nanoparticles. The size of WO_3 can be controlled by controlling the deposition condition such as evaporation pressure and substrate temperature. XRD and SEM are utilized for quantify the WO_3 products. Various sizes of WO_3 nanoparticles with size from 9 to 57 nm were formed, having monoclinic structure. It is expected that the synthesized WO_3 films by the present method has been exposed to tensile stress during the evaporation. The thermal behavior of WO_3 resistance was observed in air atmosphere as well as in NO_2 gas. For the small particle, the resistance is significantly depending on temperature at lower temperatures working, while it is temperature-independent at higher temperatures. The thermal behavior of WO_3 resistance, is confirming the competition between oxygen species and capture electrons. The change of sensor response in is harmonically correlated with the thermal behavior of resistance, the response first increased to high value in the region of temperature-dependent of resistance, while it decreased gradually in the region of temperature-independent of resistance. This behavior and correlation were ascribed to the transformation of adsorbed oxygen and nitrogen dioxide to different species.

Acknowledgements

This work funded by DeanShip of scientific research (DSR), King Abdulaziz University, Jeddah, under grant No. (662-371-D1433). The authors thank DSR technical and financial support. The authors would like deeply to thank Prof. Toshinari Yamazaki, University of Toyama Japan for his helpful discussion and FE-SEM observation.

References

- [1] Y. Baek, K. Yong, The Journal of Physical Chemistry C, **111**(3), 1213 (2007).

- [2] L. Chen, D. Weng, Z. Si, X. Wu, *Progress in Natural Science: Materials International*, **22**(4), 265 (2012).
- [3] Y. F. Dong, L. Y. Li, W. F. Jiang, H. Y. Wang, X. J. Li, *Physica E: Low-dimensional Systems and Nanostructures*, **41**(4),711(2009).
- [4] P. Tägtström, U. Jansson, *Thin Solid Films*, **352** (1), 107 (1999).
- [5] S. H. Baeck, K. S. Choi, T. F. Jaramillo, G. D. Stucky, E. W. McFarland, *Advanced Materials*, **15** (15), 1269 (2003) .
- [6] M. Yang, N. K. Shrestha, P. Schmuki, *Electrochemistry Communications*, **11**(10), 1908 (2009) -1911.
- [7] F. Mitsugi, E. Hiraiwa, T. Ikegami, K. Ebihara, R. K. Thareja, *Japanese journal of applied physics*, **41** (8R), 5372 (2002).
- [8] B. Son, W. Yang, P. Breysse, T. Chung, Y. Lee, *Environmental research*, **94** (3), 291 (2004).
- [9] World Health Organization. Health aspects of air pollution with particulate matter, ozone and nitrogen dioxide: report on a WHO working group, Bonn, Germany 13-15 January (2003).
- [10] H. Kawasaki, J. Namba, K. Iwatsuji, Y. Suda, K. Wada, K. Ebihara, T. Ohshima, *Applied surface science*, **197**,547 (2002).
- [11] R. Boulmani, M. Bendahan, C. Lambert-Mauriat, M. Gillet, K. Aguir, *Sens. Actuators B* **125**,622 (2007).
- [12] M. Stankova, X. Vilanova, E. Llobet, J. Calderer, C. Bittencourt, J. J. Pireaux, X. Correig, *Sensors and Actuators B: Chemical*, **105**(2), 271 (2005).
- [13] A. Ponzoni, E. Comini, M. Ferroni, G. Sberveglieri, *Thin Solid Films* **490**,81 (2005).
- [14] D. Meng, T. Yamazaki, Y. Shen, Z. Liu, T. Kikuta, *Applied surface science*, **256**(4), 1050 (2009).
- [15] N. Van Hieu, H. Van Vuong, N. Van Duy, N. D. Hoa, *Sensors and Actuators B: Chemical*, **171**, 760 (2012).
- [16] G. Zhang, M. Liu, *Sensors and Actuators B: Chemical*, **69**(1), 144 (2000).
- [17] N. Yamazoe, K. Shimano, *Sensors and Actuators B: Chemical*, **138**(1), 100 (2009).
N. Yamazoe, K. Shimano, *Thin Solid Films*, **517**(22), 6148 (2009).
- [18] N. Yamazoe, K. Shimano, *Sensors and Actuators B: Chemical*, **187**, 162 (2013).
- [19] S. Seal, S. Shukla, *JOM*, **54**(9), 35 (2002).
- [20] N. Yamazoe, K. Shimano, *Journal of the Electrochemical Society*, **155**(4), J85 (2008).
- [21] A. R. Bushroa, R. G. Rahbari, H. H. Masjuki, M. R. Muhamad, *Vacuum*, **86**(8), 1107 (2012).
- [22] H. Savaloni, M. Gholipour-Shahraki, M. A. Player, *Journal of Physics D Applied Physics*, **39**, 2231 (2006).
- [23] A. L. Ortiz, L. Shaw, *ActaMaterialia*, **52**(8), 2185 (2004).
- [24] J. I. Langford, A. J. C. Wilson, *Journal of Applied Crystallography*, **11**(2), 102 (1978).
- [25] F. H. Chung, D.K. Smith, *Industrial applications of X-ray diffraction*. New York: Marcel Dekker; 1999.p. 798.
- [26] R. I Masel, *Principles of Adsorption and Reaction on Solid Surfaces*, Wiley–Interscience, New York, 1996.
- [27] E. Comini, V. Guidi, C. Malagu, G. Martinelli, Z. Pan, G. Sberveglieri, Z. L. Wang, *The Journal of Physical Chemistry B*, **108**(6), 1882 (2004).
- [28] N. M. Shaalan, T. Yamazaki, T. Kikuta, *Sensors and Actuators B: Chemical*, **153**(1), 11 (2011) .
- [29] N. Yamazoe, K. Shimano, C. Sawada, *Thin Solid Films*, **515**(23), 8302 (2007).
- [30] B. Ruhland, T. Becker, G. Müller, *Sensors and Actuators B: Chemical*, **50**(1), 85 (1998).